Li, H., Peng, Q., Tang, R., Zhang, H., Zhong, Z., Deng, X., Wang, D. (2020): Statistical Characteristics of Electron Pitch Angle Distributions Inside the Magnetopasue Based on MMS Observations. - Journal of Geophysical Research: Space Physics, 125, 10, e2020JA028291.

https://doi.org/10.1029/2020JA028291

JGR Space Physics

RESEARCH ARTICLE
10.1029/2020JA028291

Statistical Characteristics of Electron Pitch Angle Distributions Inside the Magnetopasue Based on MMS Observations

Haimeng Li[1,2], Qianshui Peng[1,2], Rongxin Tang[1,2,3], He Zhang[1], Zhihong Zhong[1], Xiaohua Deng[1], and Dedong Wang[4]

[1]Institute of Space Science and Technology, Nanchang University, Nanchang, China, [2]Department of Physics, School of Science, Nanchang University, Nanchang, China, [3]Jiangxi Provincial Key Laboratory of Interdisciplinary Science, Nanchang University, Nanchang, China, [4]GFZ German Research Centre for Geosciences, Potsdam, Germany

Key Points:
- Statistical results of electron PADs inside the Earth's magnetopause based on MMS observations are presented
- Pancake PAD mainly locates at lower *L*-shell with maximum occurrence rate in noonside; other types of PAD mainly occur at higher *L*-shell
- The occurrence rates of electron PADs depending on P_{dyn} are different at different energy levels

Correspondence to:
R. Tang,
rongxint@ncu.edu.cn

Citation:
Li, H., Peng, Q., Tang, R., Zhang, H., Zhong, Z., Deng, X., & Wang, D. (2020). Statistical characteristics of electron pitch angle distributions inside the magnetopasue based on MMS observations. *Journal of Geophysical Research: Space Physics*, *125*, e2020JA028291. https://doi.org/10.1029/2020JA028291

Received 1 JUN 2020
Accepted 22 SEP 2020
Accepted article online 2 OCT 2020

Abstract Electron pitch angle distributions (PADs) are very important to understand dynamics in the Earth's magnetosphere. Using observations of the Magnetospheric Multiscale (MMS) mission, we statistically investigate the characteristics of several types of electron PADs with energies of 200 eV to 2 keV (low energy) and 2–30 keV (energetic energy) inside the dayside magnetopause ($L = 8 \sim 13$). For the low (energetic) energy level, the occurrence rates of pancake, flat-top, butterfly, isotropy, cigar, and rolling-pin distributions are as follows: 50.34% (45.20%), 17.92% (43.41%), 3.07% (7.28%), 4.34% (1.54%), 16.20% (1.20%), and 1.80% (0.06%), respectively. The pancake PAD is mainly located at lower *L*-shells with a maximum rate near the noonside, but other types of electron PADs occur at higher *L*-shells. In addition, the occurrence rate of the flat-top PAD is nearly the same for different magnetic local time. The butterfly and rolling-pin PADs occur in the afternoon side. The cigar PAD is mostly located in both the dawnside and duskside but is very scarce in the noonside. Furthermore, the relationships between these PADs and the solar wind dynamic pressure (P_{dyn}) are studied. For low-energy electrons, the occurrence rate of the pancake distribution decreases, and that of the butterfly distribution increases with the enhancement of P_{dyn}. However, for energetic energy level, the occurrence rate of the pancake (butterfly) PAD does not clearly decrease (increase) with the enhancement of P_{dyn} at $L \leq 12$. The statistical results reveal the important role of P_{dyn} in electron dynamics inside the magnetopause.

1. Introduction

Since electron dynamics in the Earth's magnetosphere are highly complex, the energetic electron flux may either increase (Miyoshi et al., 2018) or decrease (Gu et al., 2020; Miyoshi et al., 2003; Su et al., 2011; Xiao et al., 2014) during strong geomagnetic activity and high solar wind dynamic pressure (P_{dyn}). There are a variety of acceleration and loss mechanisms that affect electron flux variations and corresponding pitch angle distributions (PADs), such as wave-particle interactions (Hua et al., 2019; Huang et al., 2015; Ni et al., 2019; Summers et al., 2007, 2009; Tang et al., 2014; H. Zhao, Ni, et al., 2019) and magnetospheric compression by enhanced solar wind activities (Ni, Xiang, et al., 2016; Shprits et al., 2006; Yuan & Zong, 2013). In such a case, the long-term statistical characteristics of different electron PADs are very important dynamic properties of energetic electrons, which provide essential indicators to understand the physical processes of electron transport, energization, and loss (Liu et al., 2020; Ni, Zou, et al., 2016; Peng et al., 2020; Shi et al., 2016; Tang & Summers, 2019; H. Zhao et al., 2018; Zhong et al., 2020).

There are several kinds of electron PADs that frequently occur in the Earth's magnetosphere including the following: (1) pancake distribution with a strong anisotropy and a flux peak around pitch angle (α) = 90° (Huang et al., 2017; Zhou et al., 2013) which is the most common type of PAD in the inner magnetosphere. It is generally related to particle inward radial diffusion (Xiao et al., 2010). As particles moves inward, the electron perpendicular momentum increases faster than the parallel component because of the conservation of electron adiabatic invariants (Schulz & Lanzerotti, 1974). It is also suggested to be associated with the whistler mode wave and electrostatic electron cyclotron harmonic wave (Horne & Thorne, 2000; Meredith et al., 1999); (2) butterfly distribution with the maximum fluxes occurs around $\alpha = 45°$ and 135°, but the minimum fluxes occur around $\alpha = 90°$, 0°, and 180° (Baker et al., 1978; Meredith et al., 2000;

Ni et al., 2015; Yang et al., 2016; H. Zhao et al., 2014). Butterfly PADs have been widely studied in both the radiation belts and the slot region, which can be caused by the nonlinear bounce resonance with magnetosonic (MS) wave (Maldonado et al., 2016; Yang et al., 2016), the nonlinear Landau resonance with oblique electromagnetic ion cyclotron wave (B. Wang et al., 2016), or the Landau/cyclotron resonance with plasmaspheric hiss (Albert et al., 2016). Especially in the region of high L-shells, the butterfly distribution may be attributed to the effects of magnetopause shadowing caused by particle drift shell splitting (Sibeck et al., 1987; West et al., 1973); (3) flat-top distribution with a nearly flat flux profile at large α that can sometimes be regarded as a transition phase between the pancake distribution and the butterfly distribution (Gannon et al., 2007). Horne et al. (2003) suggested that the flat-top distribution is probably related to wave-particle interactions in the recovery phase of geomagnetic activity; (4) isotropy distribution with the nearly same flux occurs from 0° to 180° (Fu et al., 2012). The shape of isotropy distribution is very similar to that of flat-top distribution. Substorm injected electrons are almost isotropic (Åsnes et al., 2005). The isotropy distribution could also result from pitch angle scattering by whistler waves at the separatrix (Fu et al., 2012; Z. Wang et al., 2019); (5) cigar distribution (also named as bidirectional PAD) with a maximum flux around $\alpha = 0°$ or/and 180° but a minimum at large α (Fu et al., 2011; Fu, Yi, et al., 2020; Huang et al., 2020; Liu, Fu, Xu, Cao, & Liu, 2017; Ni et al., 2020; Zhou et al., 2019); it is probably a result of Fermi acceleration contributed by the compression of magnetic field line (Angelopoulos & Fu, 2016); (6) rolling-pin distribution with electron fluxes mainly at $\alpha = 0°$, 90°, and 180° (Fu, Zhao, et al., 2020; Liu, Fu, Xu, Wang, et al., 2017; M. J. Zhao, Fu, et al., 2019) that is due to both global-scale Fermi acceleration and local-scale betatron acceleration (Liu, Fu, Xu, Wang, et al., 2017).

However, previous studies have mainly focused on the characteristics of PADs in the core regions of the Earth's inner magnetosphere and magnetotail (Gannon et al., 2007; Gu et al., 2011; H. Li et al., 2015; Shi et al., 2016; H. Zhao et al., 2014, 2018). Ni, Zou, et al. (2016) investigated the occurrence rate of the butterfly PAD of outer-zone relativistic electrons and its relationship with P_{dyn} using the observations of Van Allen Probes. Yue et al. (2017) statistically analyzed several types of H^+ PADs in the inner magnetosphere. Liu et al. (2020) presented the statistical characteristics of electrons PADs (isotropy, pancake, cigar, butterfly, and rolling pin) in the magnetotail using Cluster II data. Compared with the PADs in the above regions, the characteristics of these PADs inside the dayside magnetopause still require more attention and further investigations. In the present study, for the first time, we adopt data from the Magnetospheric Multiscale (MMS) mission to statistically analyze the occurrence rate of six electron PADs (pancake, flat-top, butterfly, isotropy, cigar, and rolling pin) at two energy levels, 200 eV to 2 keV and 2–30 keV, from $L \sim 8$ to 14. Furthermore, variations of the occurrence characteristics of these PADs corresponding to P_{dyn} are investigated in detail to explore the potential causative mechanisms of different electron PADs.

The paper is organized as follows. The data and methodology used in our statistical analysis are described in section 2. Sections 3 and 4 present the global features of six typical PADs and corresponding variations based on P_{dyn}. We present discussions in section 5 and summarize the main conclusions in section 6.

2. Data Set and Methodology

On 12 March 2015, National Aeronautics and Space Administration (NASA) launched the MMS mission to investigate the physical process in the boundary regions of the Earth's magnetosphere (Burch et al., 2016). The orbits of MMS frequently cross the subsolar point between ~8 $\sim$ 13 R_E (R_E is the Earth's radius) near the magnetic equator. Fast Plasma Instrument (FPI) onboard the MMS can provide the electron flux with different α in three energy levels (<200 eV, 200 eV to 2 keV, and 2–30 keV), density, and temperature (Pollock et al., 2016). As the differential electron fluxes with energy below 200 eV was contaminated by photoelectron in some pitch angles. The differential electron fluxes may be not accurate in some pitch angles. So in this study, we mainly focus on the electron distribution and occurrence rate of PADs at two energy channels, 200 eV to 2 keV (named as low energy level in the study) and 2–30 keV (named as energetic energy level), respectively (Pollock et al., 2016). The corresponding resolution of (α) is 6°, and the time resolution is approximately 4.5 s. The data from September 2015 to December 2019 when the orbits of MMS1 were in the dayside are adopted. During this interval, the orbits of the MMS1 covered the most region in the dayside from $L \sim 8$ to $L \sim 13$, which provides good opportunity to study the electron PADs within the magnetopause. To accurately present the location of the MMS satellite in L-MLT (MLT is magnetic local

Table 1
Criteria to Define the Type of Electron PAD Based on the BI and β Indexes

Comparing	Ratio 1	Ratio 2	Type of PAD
$G < F, F < C$	$BI < 0.95$	$\beta < 0.95$	Pancake
$G < F, F \approx C$	$0.95 \leq BI \leq 1.05$	$\beta < 0.95$	Flat top
$G < F, F > C$	$BI > 1.05$	$\beta < 0.95$	Butterfly
$G \approx F, F \approx C$	$0.95 \leq BI \leq 1.05$	$0.95 \leq \beta \leq 1.05$	Isotropy
$G > F, F > C$	$BI > 0.95$	$\beta > 1.05$	Cigar
$G > F, F < C$	$BI < 0.95$	$\beta > 1.05$	Rolling pin

time) coordinates, the L and MLT are calculated by the International Geomagnetic Reference Field (IGRF) and T96 external model (Tsyganenko, 1995). Furthermore, the data of P_{dyn} are obtained by the OMNI data (1-min resolution), which is public on the Space Physics Data Facility (SPDF) of NASA's Goddard Space Flight Center database (King & Papitashvili, 2005).

Since the MMS satellites frequently cross the boundary of magnetosheath and magnetosphere, in order to investigate the electron PADs within the magnetosphere (while $L \geq 8$), we need to exclude the regions in the magnetosheath according to the characteristics of local plasma parameters. As far as we know, the electron density (N_e) in the magnetosheath is much higher than that within the magnetopause (Kim et al., 2018; Le et al., 2018; Palermo et al., 2010). Based on the model of N_e inside the magnetopause provided by Denton et al. (2004), the N_e near the magnetic equator within magnetopause is less than 3.6 cm^{-3}, while L-shell ≥ 8. In addition, the characteristics of electron energy on two sides of magnetopause are obvious different. The typical electron energy in the magnetosheath is between tens of eV and hundreds of eV, which is much lower than the typical electron energy (from several keV to tens of keV) in the magnetosphere (Huang et al., 2017). Referencing the above model and criterion, the region satisfied with the following condition is considered to locate at the inner side of the magnetopause: (1) The N_e must be less than 4 cm^{-3}, and the background electron temperature (T_e) is higher than 120 eV, which are the typical temperatures in the boundaries of the magnetosphere in our database. (2) In addition, the mean of differential electron flux with energies from 1,312 to 12,297 eV is larger than that with energies from 31 to 378 eV. Through analysis of the database, we find that the regions in the magnetosheath and boundary layer can be validly excluded using the criteria above.

To identify the type of electron PAD in the radiation belts and magnetotail, Ni, Zou, et al. (2016) and Liu et al. (2020) defined their criteria by using the flux ratio between different α. In this research, we use a similar method to classify different types of electrons PADs. The criteria are described as follows:

1. To ensure that the equatorially mirroring electrons are considered, MMS1 locations are limited within 15° of the magnetic equator.
2. Only those electron PADs that are nearly symmetric on the two sides of $\alpha = 90°$ are considered as one type of PADs mentioned above. The PADs with obvious asymmetry are therefore listed as the other type of PAD.
3. We assume that the index $G = j(a)$ is the average of electron flux between 3° and 15° (for small α); $F = j(b)$ is the average of electron flux between 27° and 69° (for medium α); $C = j(c)$ is the average of electron flux between 87° and 93° (for large α).
4. We define two indexes of flux ratio between different pitch angle α: $BI = F/C$ and $\beta = G/F$. Similar with the BI index introduced by Ni, Zou, et al. (2016), when $BI > 1.05$ and $\beta < 0.95$, the electron PAD is considered as the butterfly distribution. Using these two indexes, the pancake, flat-top, isotropy, cigar and rolling-pin PADs can also be clearly defined, as listed in Table 1.

Figure 1 shows a typical example of MMS1 observation selected by the above criterion. On 1 September 2015, MMS1 was located at afternoon side and a high L-shell region from 17:05 to 17:15 UT. During this interval, the background N_e (Figure 1a) was approximately 0.3 cm^{-3}, the electron temperature T_e (Figure 1b) is approximately 600 eV, and the electron flux with energies from 1,312 eV to 13 keV were significantly larger than that with energies from 31 to 378 eV (Figure 1c). These observations clearly suggest that the spacecraft was located inside the magnetopause. Furthermore, the electron PADs with energies from 200 eV to 2 keV are presented in Figure 1d. As shown, the electron flux exhibits an obvious butterfly distribution because the fluxes with medium α is higher than fluxes with small and large α. Using the criterion above, the corresponding BI and β indexes are plotted in Figure 1e. It is very clear that $BI > 1.05$ and $\beta < 0.95$, which indicates that the distribution is the butterfly PAD. The BI index increases when the butterfly distribution is more obvious. On the other hand, Figure 1f shows the electron flux with energy 2–30 keV. The electrons at energetic energy level undergo three different types of PADs (pancake, butterfly, and flat-top distributions denoted by pink, purple, and yellow shadows, respectively), which can also be determined by the values of BI and β

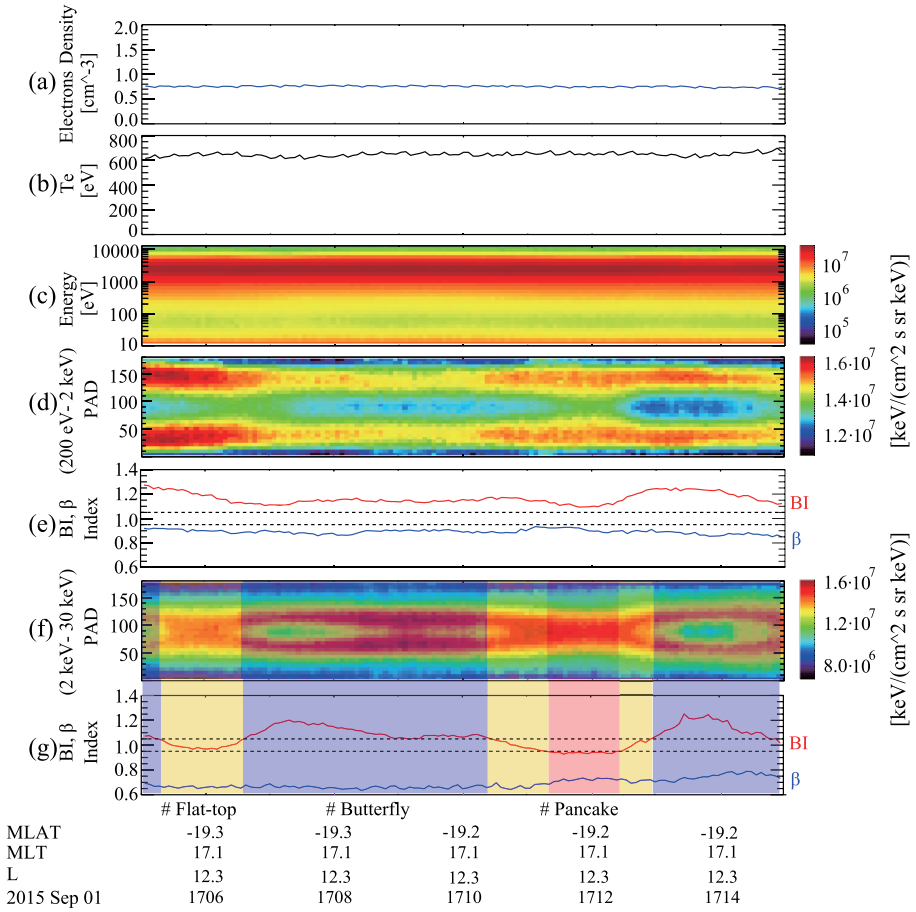

Figure 1. A typical example of MMS1 observation selected inside the magnetopause by the above criterion from 17:05 to 17:15 UT on 1 September 2015: (a) background electron density N_e, (b) electron temperature T_e, (c) electron flux from 31 to 12,297 eV, (d) electron PAD with energy from 200 eV to 2 keV, (e) the calculated *BI* and β indexes for Figure 1d, (f) electron PAD with energy from 2 to 30 keV, and (g) the calculated *BI* and β indexes for Figure 1f. The pancake, butterfly, and flat-top distributions are denoted by pink, purple, and yellow shadows, respectively.

indexes, as shown in Figure 1g. This example clearly implies that the criterion mentioned above can well justify the types of electron PADs.

3. Global Features of PADs Inside the Magnetopause

Based on above criterion of electron PADs, the region of statistical analysis is confined to L ~ 8–13 inside the dayside magnetopause. Since the time resolution of electron differential flux provided by FPI data is ~4.5 s, the type of PAD sample is defined every 4.5 s. There are a total number of 99,050 samples inside the dayside magnetopause (near magnetic equator) that are statistically analyzed. Figure 2a presents the number of valid case samples inside the magnetopause as a function of L-shell and MLT (each bin is defined by 0.5 L-shell and 1 MLT). To ensure the reliability of the statistical results, the bin where the number of samples is below 50 is ignored and defined as blank. Valid case samples seem to cover most regions of L ~ 8–12 in the dayside magnetosphere. Nevertheless, the valid samples from L ~ 12 to 13 are mainly located near the duskside (from MLT = 16 to 19). Figures 2b and 2c show the corresponding occurrence rates of different types of electron PADs based on valid samples for two energy levels. For the low energy level (from 200 eV to 2 keV), the pancake distribution is most prevalent at approximately 50.34%. The occurrence rates of flat-top (17.92%) and cigar (16.20%) distributions are similar. However, the occurrence rates of the butterfly (3.07%), isotropy (4.34%), and rolling-pin (1.80%) distributions are very scarce. Interestingly, there are also a number of

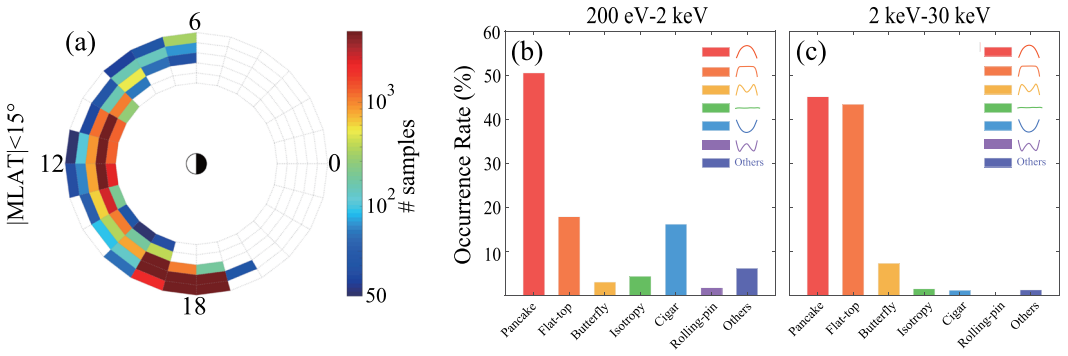

Figure 2. (a) All valid case samples of MMS1 in the L-MLT coordinate for $L = 8$–14. (b) Occurrence rates of different PADs for the electron with energies from 200 eV to 2 keV. (c) Occurrence rates of different PADs for the electron with energies from 2 to 30 keV are calculated based on all valid cases in each bin. Since the difference of these types of electron PADs is extremely variable, we use different colorbar ranges in different panels.

electron PADs with asymmetrical or illegible shapes, which are listed as the other type of PADs (6.13%) in Figure 2b. This may be caused by some open magnetic field line topology inside magnetopause, for example, the flux rope, to form a channel and transfer the low-energy electrons between the magnetosheath and the magnetosphere (Man et al., 2020; Zhang et al., 2008). For the energetic energy level (from 2 to 30 keV), the occurrence rates of flat-top (43.41%) and butterfly (7.28%) distributions clearly increase. The rate of the flat-top distribution even approaches that of the pancake (45.20%) distribution. Moreover, the isotropy, cigar, rolling-pin, and other distributions become much less. The detailed values are listed in Table 2.

To further analyze the variation of different PADs depending on different L-shell and MLT, the global distributions of the occurrence rates for six electron PADs at the low energy level (200 eV to 2 keV) from $L = 8$ to 13 are shown in Figure 3. Each bin is also defined by 0.5 L-shell and 1 MLT, and the corresponding occurrence rate is calculated based on all valid cases in each bin. Since the difference of these types of electron PADs are extremely variable, we use different colorbar ranges in different panels.

The results clearly show that the pancake PAD was primarily distributed at lower L-shell and is the most predominant PAD within $L \leq 10$. Its occurrence rate clearly decreases with the enhancement of the L-shell. In addition, the occurrence rate of the pancake PAD near noon is much higher than that in the dawnside and duskside. Compared with the pancake PAD, the flat-top, butterfly, isotropy, and cigar PADs mainly occur at higher L-shells ($L > 10$). Furthermore, the flat-top PAD occurs in both the prenoon and afternoon sides. The isotropy and cigar PADs can be found in the dawnside and duskside. Nevertheless, the butterfly PAD mainly occurs in the afternoon side. The occurrence rate of the rolling-pin PAD is the least and is mainly located within lower L-shell region.

Since the occurrence rates of isotropy, cigar, and rolling-pin PADs at energetic energy level (2–30 keV) are very small (also see Figure 2c), Figure 4 only presents the global occurrence rates of the pancake, flat-top, and butterfly PADs for energetic energy electrons. In such a case, the occurrence rate of the pancake PAD is largest near the noonside with low L-shell, which is very similar to cases at low energy level. However, the higher occurrence rate of the pancake PAD can extend to the region with high L-shells and is different from the results presented in Figure 3a (low energy level). The global distribution of the flat-top PADs shows an independent relation with MLT, and its occurrence rate varies little with respect to different MLT values. Furthermore, the butterfly PAD mainly occurs in the afternoon side. Compared to the cases at low energy

Table 2
Occurrence Rates of Different Types of Electron PADs Based on All Valid Case Samples

Energy level	Pancake	Flat top	Butterfly	Isotropy	Cigar	Rolling pin	Other
200 eV to 2 keV	50.34%	17.92%	3.07%	4.34%	16.20%	1.80%	6.13%
2–30 keV	45.20%	43.41%	7.28%	1.54%	1.20%	0.06%	1.30%

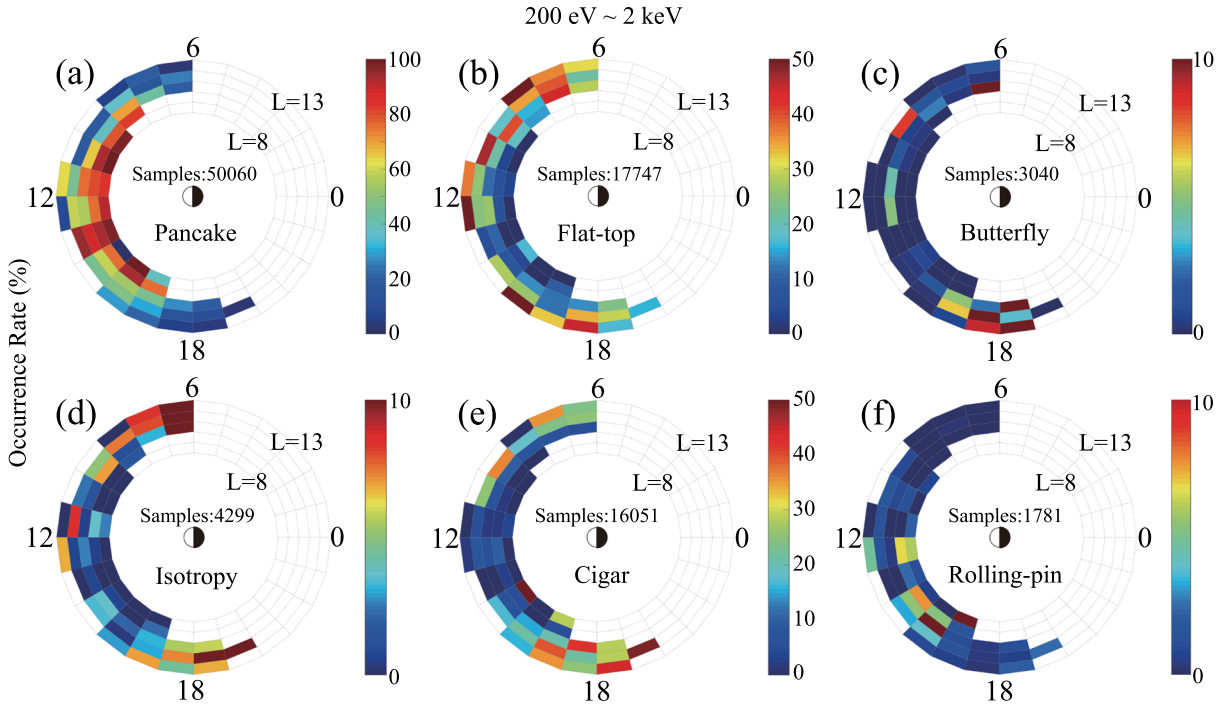

Figure 3. Occurrence rates of six typical electron PADs as a function of *L*-shell and MLT for the electron with energy from 200 eV to 2 keV: (a) pancake, (b) flat-top, (c) butterfly, (d) isotropy, (e) cigar, and (f) rolling-pin distributions.

level, high occurrence rates of both flat-top and butterfly PADs can significantly extend to the region with lower *L*-shells.

4. Variation of Typical PADs Depending on P_{dyn}

When the solar wind condition becomes highly intensified, the Earth's magnetosphere can be compressed inward, which leads to electron acceleration (Yu et al., 2016). Magnetopause shadowing contributed by a strong P_{dyn} can also cause the electron drift shell splitting and result in the electron loss at larger α (X. Li et al., 1997). These competition mechanisms can bring different effects on the evolution process and final results of electron PADs inside the magnetopause. To investigate the potential correlation between PADs and P_{dyn} at different *L*-shells in detail, the occurrence rates of several important PADs with respect to P_{dyn} (indicated $8 \le L \le 10$, $10 \le L \le 12$, and $12 \le L \le 13$) at two energy channels are presented in Figures 5 and 6, respectively.

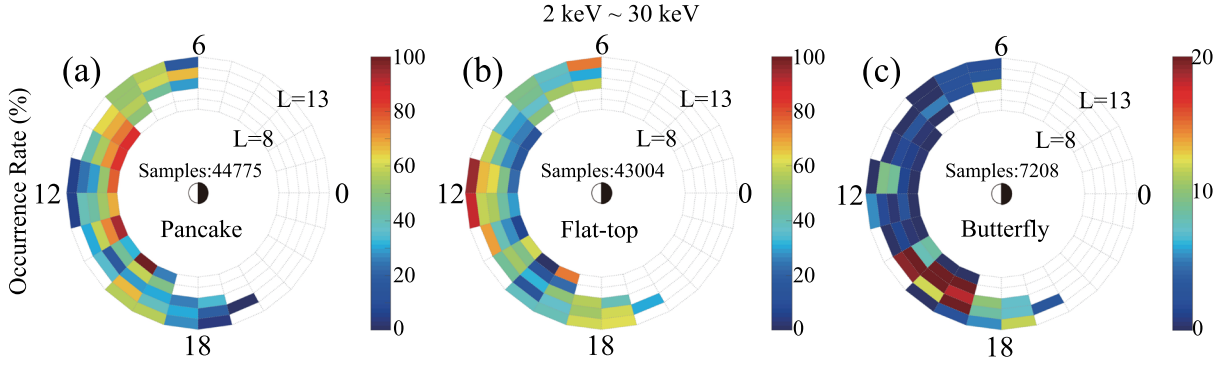

Figure 4. Occurrence rates of three typical electron PADs as a function of *L*-shell and MLT for the electron with energy from 2 to 30 keV: (a) pancake, (b) flat-top, and (c) butterfly distributions.

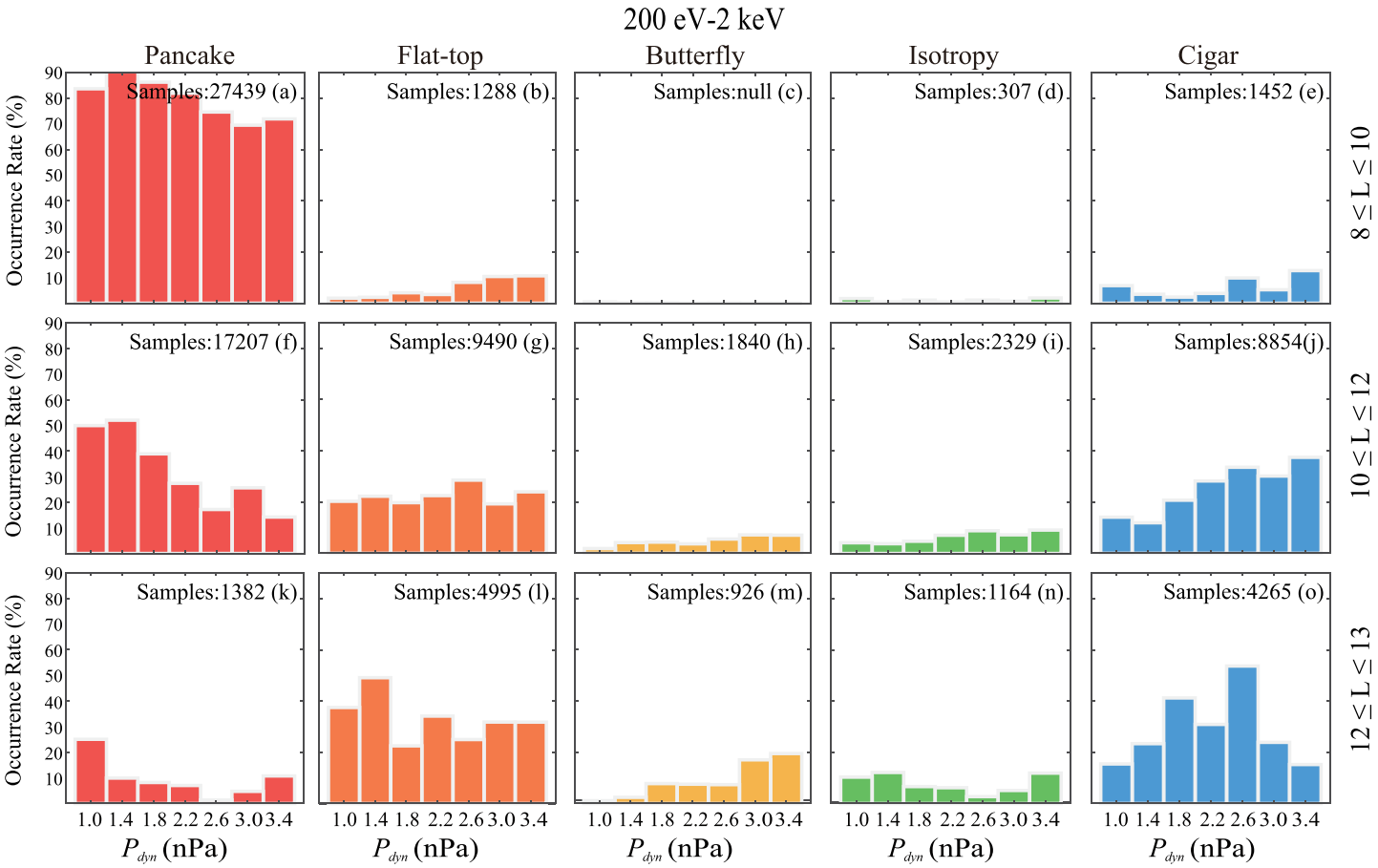

Figure 5. Occurrence rates of five typical PADs for the low-energy electrons (200 eV to 2 keV) as a function of P_{dyn} for indicated L-shell regions. The column panels from left to right are (a, f, and k) pancake, (b, g, and l) flat-top, (c, h, and m) butterfly, (d, i, and n) isotropy, and (e, j, and o) cigar PADs, respectively.

As shown in Figure 5, for electrons at lower energy level (the occurrence rate variation of rolling-pin PAD is excluded, because its occurrence rate is too little), the pancake PAD similarly behaves the most prevalent type inside the magnetopause within $L \leq 10$. Its occurrence rate decreases as the enhancement of P_{dyn} for all three L-shell regions. On the other hand, the butterfly PAD mainly concentrates on the higher L-shell regions ($10 \leq L \leq 13$), and its occurrence rate dramatically increases when the P_{dyn} increases. The variations of the occurrence rates of pancake and butterfly PADs indicate that the electron loss with larger α with the enhancement of P_{dyn}. The occurrence rate of the flat-top PAD remains relatively stable with respect to the P_{dyn}. The flat-top PAD is similar to a transition stage between the pancake and butterfly PADs. The occurrence rate of the isotropy PAD exhibits a positive correlation with the enhancement of P_{dyn} at $10 \leq L \leq 12$ but shows no positive correlation at $12 \leq L \leq 13$. Furthermore, the occurrence rate of the cigar PAD is positively correlated with P_{dyn} at $10 \leq L \leq 12$ and at $12 \leq L \leq 13$ when $P_{dyn} \leq 2.6$ nPa.

Since the occurrence rates of isotropy, cigar, rolling-pin and other PADs are too small, Figure 6 only shows variations of the occurrence rates of the pancake, flat-top, and butterfly PADs at energetic energy level (2–30 keV) as a function of P_{dyn} for the indicated L-shell regions. The characteristics of pancake, flat-top, and butterfly PADs with respect to P_{dyn} when $L \leq 12$ for the energetic energy electrons are somehow different from those for the low-energy electrons. As shown in Figures 6a and 6d, the occurrence rates of the pancake PAD do not exhibit an obvious decrease with the enhancement of P_{dyn} while $L \leq 12$. Furthermore, there is no obvious positive or negative correlation between the occurrence rate of butterfly PAD and P_{dyn} at $8 \leq L \leq 10$ (shown in Figure 6c). Figure 6i shows that the occurrence rate of the butterfly PAD decreases with the enhancement of P_{dyn} (when $P_{dyn} \leq 3.2$ nPa) while $10 \leq L \leq 12$. In the region with $12 \leq L \leq 13$, the occurrence rate of the pancake PAD decreases; on the other hand, the occurrence rate of the butterfly PAD

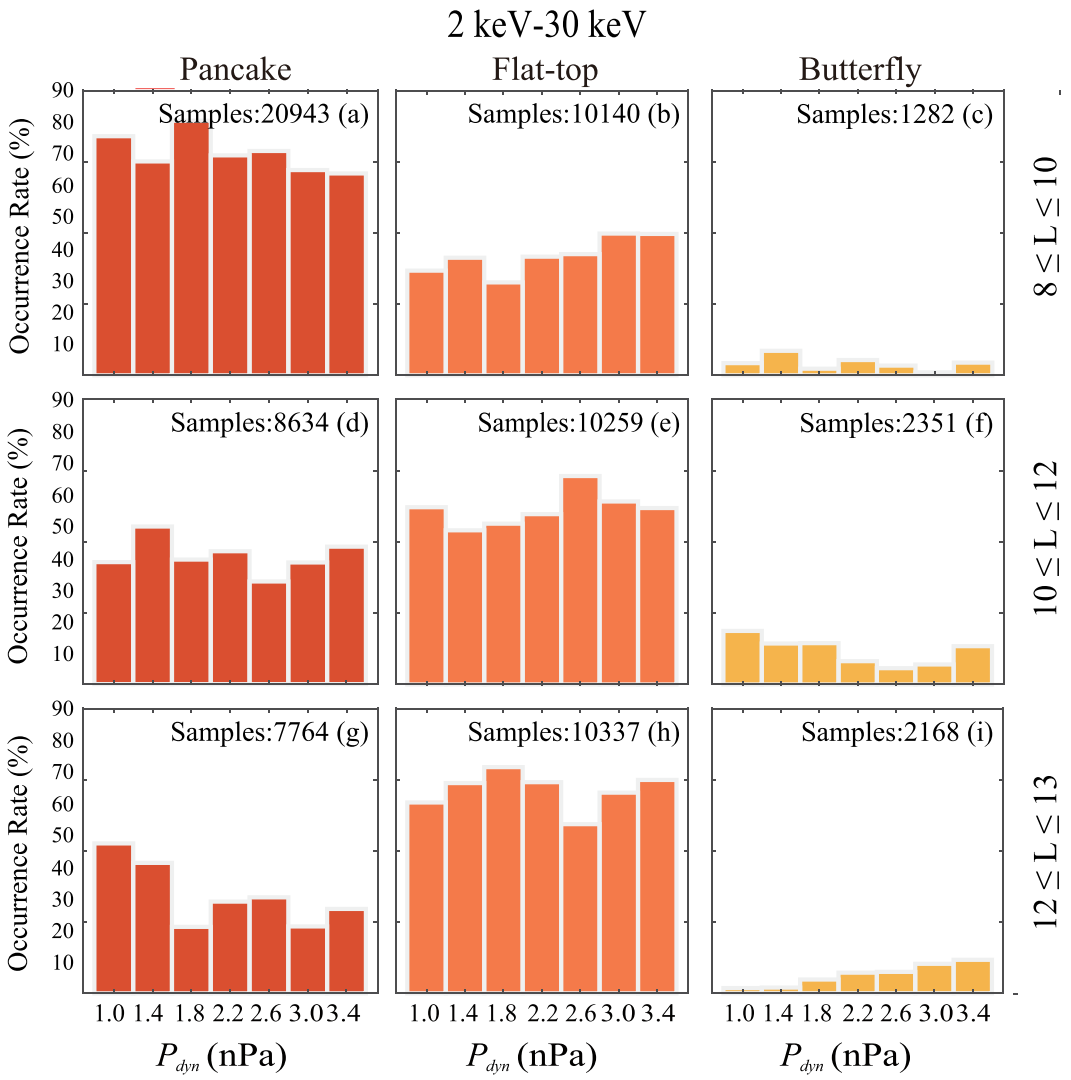

Figure 6. Occurrence rates of five typical PADs for the energetic energy electrons (2–30 keV) as a function of P_{dyn} for indicated L-shell regions. The column panels from left to right are (a, d, and g) pancake, (b, e, and h) flat-top, and (c, f, and i) butterfly PADs, respectively.

increases with the enhancement of P_{dyn}. It is noteworthy that, in the region with $12 \leq L \leq 13$, the number of samples from MLT = 6 to MLT = 16 is relatively low, and the samples are mainly located near duskside (from MLT = 16 to MLT = 19). As a result, Figures 6g–6i primarily reflect the variation of occurrence rate with $12 \leq L \leq 13$ near the duskside.

5. Discussions

The statistical results suggest that the occurrence rates of the cigar and isotropy PADs are very scarce for electrons at energetic energy level but relatively large at low energy level (also shown in Table 2). The cigar PAD frequently occurs in the dawnside and duskside, which indicates that these bidirectional field-aligned warm electrons may originate from ionospheric polar wind (Chappell et al., 2008) and can be considered as upgoing electron beams accelerated by the diverging electric field (Abel et al., 2002; Yue et al., 2017). Abel et al. (2002) also suggested that this type of bidirectional electron event is an occurring phenomenon in the magnetosphere. It is often associated with electrostatic shock, field-aligned currents and possibly auroral arcs. Furthermore, as shown in Figure 5, it seems that the occurrence rate of the cigar PAD increases with the enhancement of P_{dyn} where $10 \leq L \leq 12$ and is relative large for $P_{dyn} > 1.2$ nPa where $12 \leq L \leq 13$.

The higher occurrence rate of the cigar PAD during stronger P_{dyn} may be because P_{dyn} is the main factor controlling the field-aligned currents (H. Wang et al., 2007). For electrons at a low energy level, the distribution of the isotropy PAD is similar to that of the flat-top PAD, but its occurrence rates are much less than those of the flat-top PAD. Since the observed isotropy PADs are mainly located in the dawn and dusk regions with high L-shells, it may be affected by the strong curvature of the stretched magnetic field in the night. The electrons having a velocity component parallel to the magnetic field are no longer able to conserve adiabatic invariants. The electron chaotic motion can cause pitch angle diffusion and bring about approximately isotropy PAD (Chen et al., 2014; Ingraham et al., 2001; Sergeev et al., 1983).

Moreover, it is clear that the pancake PAD is the most prevalent type inside the magnetopause within $L \leq 10$ for electrons with both energy levels. It is very similar to the characteristics of the energetic electron PAD in the inner magnetosphere. The most common type of PAD is thought to form as a consequence of either electrons with small α loss to the atmosphere combined with wave-particle interaction or pitch angle diffusion (H. Zhao et al., 2014).

For electrons at low energy level, the occurrence rate of pancake PAD decreases with the enhancement of P_{dyn}. This could be explained by the magnetopause shadowing (X. Li et al., 1997) associated with magnetopause compression. The day-night magnetic field asymmetry is obvious at high L-shells, so in order to conserve the first adiabatic invariant, particles with larger α can drift to the outer L-shell region when they drift from nightside to dayside. This mechanism is also called drift shell splitting (Roederer, 1970; Selesnick & Blake, 2002). Therefore, particles with larger α will drift and be lost outside the magnetopause. Moreover, the enhanced P_{dyn} can further strike the magnetopause and cause an increase of the dayside magnetic field but reduction of the nightside magnetic field, which will result in more electron losses with α near 90°, leading to a decrease in the occurrence pancake PADs.

On the other hand, as P_{dyn} is enhanced, drift loss occurs to electrons with α near 90° by magnetopause shadowing, especially in the noonside. Thus, butterfly PADs frequently occur in the afternoon side at higher L-shells. Although butterfly PADs can also be contributed by electron pitch angle scattering approximately 90° due to MS waves, the spatial range of a butterfly PAD is not consistent with that of MS reported by Ma et al. (2013). We believe that drift shell splitting and the corresponding magnetosphere compression caused by enhanced P_{dyn} could be the main factor for the increased occurrence butterfly PADs.

Interestingly, for electrons at energetic energy level (2–30 keV), the corresponding variation as a function of P_{dyn} exhibits different characteristics. While $L \leq 12$, as P_{dyn} is enhanced, pancake, and butterfly PADs do not occur more frequently. These features present similar statistical energetic electron PAD characteristics in the core region of the outer radiation belt to those reported by Yu et al. (2016), which indicates that higher energy electrons have stronger anisotropy. It demonstrates electron acceleration at α with the enhancement of P_{dyn}. One candidate explanation is that, for preserving the first adiabatic invariant, the electron perpendicular energy is due to strong compression of the dayside magnetic field. In such a case, the role of the acceleration mechanism may exceed or be equal that of the loss mechanism due to drift shell splitting.

6. Conclusions

In this paper, FPI measurements on board MMS1 from September 2015 to December 2019 are used to presented a detailed statistical study on electron PADs within the dayside magnetopause ($L \sim 8$–13) for two energy levels, 200 eV to 2 keV and 2–30 keV, respectively. Six different types of the electron PADs are identified via two flux ratios between different pitch angles. The main conclusions are as follows:

1. For the electrons at both energy levels, the pancake PAD mainly occurs at the lower L-shell region and is most predominant within $L \leq 10$. Its occurrence rate clearly decreases with the increase of L-shell, especially for low-energy electrons. The occurrence rate of the pancake PAD in the noonside is also higher than those in the dawnside and duskside.
2. Compared with the pancake PAD, other types of electron PADs generally occur at higher L-shells. The flat-top PAD occurs in both the prenoon and afternoon sides, and its occurrence rate is nearly the same for different MLT values. On the other hand, the butterfly PAD typically occurs in the afternoon side.

3. The occurrence rates of cigar, isotropy, and rolling-pin PADs are very scarce for electrons at energetic energy level. Nevertheless, the occurrence rates of cigar and isotropy PADs are relatively large for electrons at low energy level. The cigar and isotropy PADs generally occur in the dawnside and duskside.
4. The occurrence rates of electron PADs inside the magnetopause exhibit an interesting relationship to P_{dyn}. For the low energy level, with the enhancement of P_{dyn}, pancake PADs occur less frequently, while butterfly PADs occur more, which suggests that the electron loss is approximately 90°. However, for the energetic energy level, the pancake (butterfly) PADs does not clearly occur more or less frequently with the enhancement of P_{dyn} at $L \leq 12$. These results statistically reveal the complex competition relationship between electron acceleration and loss depending on P_{dyn}. Furthermore, the flat-top PAD may be a transition phase between the pancake PAD and the butterfly PAD. There is also a nearly positive correlation between the occurrence rate of cigar PADs and P_{dyn}.

Since electron PADs significantly reflect the source, transport, and loss of energetic electrons at different energies, in the present study, the global distributions of six types of electron PADs depending on L-shell, MLT, and P_{dyn} parameters are investigated in detail, which is important to further understand the evolution mechanisms of these electron PADs. More comparisons with theoretical modeling and computer simulations will be studied in our next project.

Data Availability Statement

Data used for this study are publicly available from the MMS Science Data Center (https://lasp.colorado.edu/mms/sdc/public/) and the OMNI website (https://spdf.gsfc.nasa.gov/pub/data/omni/omni.cdaweb/hro1min/).

Acknowledgments
This work was supported by National Natural Science Foundation of China (NSFC) under grant Nos. 42064009, 41974195, 41674144, and 41604156, Interdisciplinary Innovation Fund of Natural Science from Nanchang University under grant No. 9166-27060003-YB14, and Youth Science Foundation of Jiangxi Province under grant No. 20171BAB213028. We appreciate the entire MMS team and MMS Science Data Center for providing the high-quality data and successful operation.

References

Abel, G. A., Fazakerley, A. N., & Johnstone, A. D. (2002). Statistical distributions of field-aligned electron events in the near-equatorial magnetosphere observed by the low energy plasma analyzer on CRRES. *Journal of Geophysical Research*, *107*(A11), 1393. https://doi.org/10.1029/2001JA005073

Albert, J. M., Starks, M. J., Horne, R. B., Meredith, N. P., & Glauert, S. A. (2016). Quasi-linear simulations of inner radiation belt electron pitch angle and energy distributions. *Geophysical Research Letters*, *43*, 2381–2388. https://doi.org/10.1002/2016GL067938

Åsnes, A., Friedel, R. W., Stadsnes, J., Thomsen, M., Østgaard, N., & Cayton, T. (2005). Statistical pitch angle properties of substorm-injected electron clouds and their relation to dawnside energetic electron precipitation. *Journal of Geophysical Research*, *110*, A05207. https://doi.org/10.1029/2004JA010838

Baker, D. N., Higbie, P. R., Hones, E. W., & Belian, R. D. (1978). High-resolution energetic particle measurements at 6.6 R_E, 3. Low-energy electron anisotropies and short-term substorm predictions. *Journal of Geophysical Research*, *83*(A10), 4863–4868. https://doi.org/10.1029/JA083iA10p04863

Burch, J. L., Moore, T. E., Torbert, R. B., & Giles, B. L. (2016). Magnetospheric Multiscale overview and science objectives. *Space Science Reviews*, *199*(1–4), 5–21. https://doi.org/10.1007/s11214-015-0164-9

Chappell, C. R., Huddleston, M. M., Moore, T. E., Giles, B. L., & Delcourt, D. C. (2008). Observations of the warm plasma cloak and an explanation of its formation in the magnetosphere. *Journal of Geophysical Research*, *113*, A09206. https://doi.org/10.1029/2007JA012945

Chen, Y., Friedel, R. H. W., Henderson, M. G., Claudepierre, S. G., Morley, S. K., & Spence, H. E. (2014). REPAD: An empirical model of pitch angle distributions for energetic electrons in the Earth's outer radiation belt. *Journal of Geophysical Research: Space Physics*, *119*, 1693–1708. https://doi.org/10.1002/2013JA019431

Denton, R. E., Menietti, J. D., Goldstein, J., Young, S. L., & Anderson, R. R. (2004). Electron density in the magnetosphere. *Journal of Geophysical Research*, *109*, A09215. https://doi.org/10.1029/2003JA010245

Fu, H. S., Khotyaintsev, Y. V., André, M., & Vaivads, A. (2011). Fermi and betatron acceleration of suprathermal electrons behind dipolarization fronts. *Geophysical Research Letters*, *38*, L16104. https://doi.org/10.1029/2011GL048528

Fu, H. S., Khotyaintsev, Y. V., Vaivads, A., André, M., Sergeev, V. A., Huang, S. Y., et al. (2012). Pitch angle distribution of suprathermal electrons behind dipolarization fronts: A statistical overview. *Journal of Geophysical Research*, *117*, A12221. https://doi.org/10.1029/2012JA018141

Fu, H. S., Zhao, M. J., Yu, Y., & Wang, Z. (2020). A new theory for energetic electron generation behind dipolarization front. *Geophysical Research Letters*, *47*(6). https://doi.org/10.1029/2019GL086790

Fu, S., Yi, J., Ni, B., Zhou, R., Hu, Z., Cao, X., et al. (2020). Combined scattering of radiation belt electrons by low-frequency hiss: Cyclotron, landau, and bounce resonances. *Geophysical Research Letters*, *47*(5). https://doi.org/10.1029/2020GL086963

Gannon, J. L., Li, X., & Heynderickx, D. (2007). Pitch angle distribution analysis of radiation belt electrons based on combined release and radiation effects satellite medium electrons a data. *Journal of Geophysical Research*, *112*, A05212. https://doi.org/10.1029/2005JA011565

Gu, X., Xia, S., Fu, S., Xiang, Z., Ni, B., Guo, J., & Cao, X. (2020). Dynamic responses of radiation belt electron fluxes to magnetic storms and their correlations with magnetospheric plasma wave activities. *The Astrophysical Journal*, *891*(2), 127. https://doi.org/10.3847/1538-4357/ab71fc

Gu, X., Zhao, Z., Ni, B., Shprits, Y., & Zhou, C. (2011). Statistical analysis of pitch angle distribution of radiation belt energetic electrons near the geostationary orbit: CRRES observations. *Journal of Geophysical Research*, *116*, A01208. https://doi.org/10.1029/2010JA016052

Horne, R. B., Meredith, N. P., Thorne, R. M., Heynderickx, D., Iles, R. H. A., & Anderson, R. R. (2003). Evolution of energetic electron pitch angle distributions during storm time electron acceleration to megaelectronvolt energies. *Journal of Geophysical Research*, *108*(A1), 1016. https://doi.org/10.1029/2001JA009165

Horne, R. B., & Thorne, R. M. (2000). Electron pitch angle diffusion by electrostatic electron cyclotron harmonic waves: The origin of pancake distributions. *Journal of Geophysical Research*, *105*(A3), 5391–5402. https://doi.org/10.1029/1999JA900447

Hua, M., Ni, B., Li, W., Gu, X., Fu, S., Shi, R., et al. (2019). Evolution of radiation belt electron pitch angle distribution due to combined scattering by plasmaspheric hiss and magnetosonic waves. *Geophysical Research Letters*, *46*, 3033–3042. https://doi.org/10.1029/2018GL081828

Huang, S. Y., Sahraoui, F., Yuan, Z. G., He, J. S., Zhao, J. S., Contel, O. L., et al. (2017). Magnetospheric Multiscale observations of electron vortex magnetic hole in the turbulent magnetosheath plasma. *The Astrophysical Journal*, *836*(2), L27. https://doi.org/10.3847/2041-8213/aa5f50

Huang, S. Y., Xu, S. B., He, L. H., Jiang, K., Yuan, Z. G., Deng, X. H., et al. (2020). Excitation of whistler waves through the bidirectional field-aligned electron beams with electron temperature anisotropy: MMS observations. *Geophysical Research Letters*, *47*(14). https://doi.org/10.1029/2020GL087515

Huang, S. Y., Yuan, Z. G., Ni, B., Zhou, M., Fu, H. S., Fu, S., et al. (2015). Observations of large-amplitude electromagnetic waves and associated wave–particle interactions at the dipolarization front in the Earth's magnetotail: A case study. *Journal of Atmospheric and Solar-Terrestrial Physics*, *129*, 119–127. https://doi.org/10.1016/j.jastp.2015.05.007

Ingraham, J. C., Cayton, T. E., Belian, R. D., Christensen, R. A., Friedel, R. H. W., Meier, M. M., et al. (2001). Substorm injection of relativistic electrons to geosynchronous orbit during the great magnetic storm of March 24, 1991. *Journal of Geophysical Research*, *106*(A11), 25,759–25,776. https://doi.org/10.1029/2000JA000458

Kim, K. H., Kim, G. J., & Kwon, H. J. (2018). Distribution of equatorial Alfvén velocity in the magnetosphere: A statistical analysis of THEMIS observations. *Earth, Planets and Space*, *70*(1), 174. https://doi.org/10.1186/s40623-018-0947-9

King, J. H., & Papitashvili, N. E. (2005). Solar wind spatial scales in and comparisons of hourly Wind and ACE plasma and magnetic field data. *Journal of Geophysical Research*, *110*, A02104. https://doi.org/10.1029/2004JA010649

Le, A., Daughton, W., Ohia, O., Chen, L. J., Liu, Y. H., Wang, S., et al. (2018). Drift turbulence, particle transport, and anomalous dissipation at the reconnecting magnetopause. *Physics of Plasmas*, *25*(6), 062103. https://doi.org/10.1063/1.5027086

Li, H., Zhou, M., Deng, X., Yuan, Z., Guo, L., Yu, X., et al. (2015). A statistical study on the whistler waves behind dipolarization fronts. *Journal of Geophysical Research: Space Physics*, *120*, 1086–1095. https://doi.org/10.1002/2014JA020474

Li, X., Baker, D. N., Temerin, M., Cayton, T. E., Reeves, E. G. D., Christensen, R. A., et al. (1997). Multisatellite observations of the outer zone electron variation during the November 3–4, 1993, magnetic storm. *Journal of Geophysical Research*, *102*(A7), 14,123–14,140. https://doi.org/10.1029/97JA01101

Liu, C. M., Fu, H. S., Liu, Y. Y., Wang, Z., Chen, G., Xu, Y., & Chen, Z. Z. (2020). Electron pitch-angle distribution in Earth's magnetotail: Pancake, cigar, isotropy, butterfly, and rolling-pin. *Journal of Geophysical Research: Space Physics*, *125*, e2020JA027777. https://doi.org/10.1029/2020JA027777

Liu, C. M., Fu, H. S., Xu, Y., Cao, J. B., & Liu, W. L. (2017). Explaining the rolling-pin distribution of suprathermal electrons behind dipolarization fronts. *Geophysical Research Letters*, *44*, 6492–6499. https://doi.org/10.1002/2017GL074029

Liu, C. M., Fu, H. S., Xu, Y., Wang, T. Y., Cao, J. B., Sun, X. G., & Yao, Z. H. (2017). Suprathermal electron acceleration in the near-Earth flow rebounce region. *Journal of Geophysical Research: Space Physics*, *122*, 594–604. https://doi.org/10.1002/2016JA023437

Lu, S., Angelopoulos, V., & Fu, H. (2016). Suprathermal particle energization in dipolarization fronts: Particle-in-cell simulations. *Journal of Geophysical Research: Space Physics*, *121*, 9483–9500. https://doi.org/10.1002/2016JA022815

Ma, Q., Li, W., Thorne, R. M., & Angelopoulos, V. (2013). Global distribution of equatorial magnetosonic waves observed by THEMIS. *Geophysical Research Letters*, *40*, 1895–1901. https://doi.org/10.1002/grl.50434

Maldonado, A. A., Chen, L., Claudepierre, S. G., Bortnik, J., Thorne, R. M., & Spence, H. (2016). Electron butterfly distribution modulation by magnetosonic waves. *Geophysical Research Letters*, *43*, 3051–3059. https://doi.org/10.1002/2016GL068161

Man, H., Zhong, Z., & Li, H. (2020). Internal structures of the ion-scale flux rope associated with dayside magnetopause reconnection. *Astrophysics and Space Science*, *365*(5), 87. https://doi.org/10.1007/s10509-020-03803-8

Meredith, N. P., Horne, R. B., Johnstone, A. D., & Anderson, R. R. (2000). The temporal evolution of electron distributions and associated wave activity following substorm injections in the inner magnetosphere. *Journal of Geophysical Research*, *105*(A6), 12,907–12,917. https://doi.org/10.1029/2000JA900010

Meredith, N. P., Johnstone, A. D., Szita, S., Horne, R. B., & Anderson, R. R. (1999). "Pancake" electron distributions in the outer radiation belts. *Journal of Geophysical Research*, *104*(A6), 12,431–12,444. https://doi.org/10.1029/1998JA900083

Miyoshi, Y., Morioka, A., Obara, T., Misawa, H., Nagai, T., & Kasahara, Y. (2003). Rebuilding process of the outer radiation belt during the 3 November 1993 magnetic storm: NOAA and Exos-D observations. *Journal of Geophysical Research*, *108*(A1), 1004. https://doi.org/10.1029/2001JA007542

Miyoshi, Y., Shinohara, I., Takashima, T., Asamura, K., Higashio, N., Mitani, T., et al. (2018). Geospace exploration project ERG. *Earth, Planets and Space*, *70*(1), 101. https://doi.org/10.1186/s40623-018-0862-0

Ni, B., Huang, H., Zhang, W., Gu, X., Zhao, H., Li, X., et al. (2019). Parametric sensitivity of the formation of reversed electron energy spectrum caused by plasmaspheric hiss. *Geophysical Research Letters*, *46*, 4134–4143. https://doi.org/10.1029/2019GL082032

Ni, B., Xiang, Z., Gu, X., Shprits, Y. Y., Zhou, C., Zhao, Z., et al. (2016). Dynamic responses of the Earth's radiation belts during periods of solar wind dynamic pressure pulse based on normalized superposed epoch analysis. *Journal of Geophysical Research: Space Physics*, *121*, 8523–8536. https://doi.org/10.1002/2016JA023067

Ni, B., Yan, L., Fu, S., Gu, X., Cao, X., Xiang, Z., & Zhang, Y. (2020). Distinct formation and evolution characteristics of outer radiation belt electron butterfly pitch angle distributions observed by Van Allen probes. *Geophysical Research Letters*, *47*, e2019GL086487. https://doi.org/10.1029/2019GL086487

Ni, B., Zou, Z., Gu, X., Zhou, C., Thorne, R. M., Bortnik, J., et al. (2015). Variability of the pitch angle distribution of radiation belt ultrarelativistic electrons during and following intense geomagnetic storms: Van Allen Probes observations. *Journal of Geophysical Research: Space Physics*, *120*, 4863–4876. https://doi.org/10.1002/2015JA021065

Ni, B., Zou, Z., Li, X., Bortnik, J., Xie, L., & Gu, X. (2016). Occurrence characteristics of outer zone relativistic electron butterfly distribution: A survey of Van Allen Probes REPT measurements. *Geophysical Research Letters*, *43*, 5644–5652. https://doi.org/10.1002/2016GL069350

Palermo, F., Califano, F., Pegoraro, F., & le Contel, O. (2010). Possible magnetospheric Kelvin-Helmholtz vortex signatures near the post-noon magnetopause. *Memorie della Societa Astronomica Italiana Supplement*, *14*, 189.

Peng, Q., Li, H., Tang, R., Zhong, Z., Zhang, H., & Li, Q. (2020). Variation of dayside chorus waves associated with solar wind dynamic pressure based on MMS observations. *Advances in Space Research*, *65*(11), 2551–2558. https://doi.org/10.1016/j.asr.2020.03.006

Pollock, C., Moore, T., Jacques, A., Burch, J., Gliese, U., Saito, Y., et al. (2016). Fast plasma investigation for Magnetospheric Multiscale. *Space Science Reviews*, *199*(1–4), 331–406. https://doi.org/10.1007/s11214-016-0245-4

Roederer, J. G. (1970). *Dynamics of geomagnetically trapped radiation*. Berlin: Springer. https://doi.org/10.1007/978-3-642-49300-3

Schulz, M., & Lanzerotti, L. J. (1974). *Particle diffusion in the radiation belts*. New York, NY: Springer. https://doi.org/10.1007/978-3-642-65675-0

Selesnick, R. S., & Blake, J. B. (2002). Relativistic electron drift shell splitting. *Journal of Geophysical Research*, *107*(A9), 1265. https://doi.org/10.1029/2001JA009179

Sergeev, V. A., Sazhina, E., Tsyganenko, N. A., Lundblad, J., & Soraas, F. (1983). Pitch-angle scattering of energetic protons in the magnetotail current sheet as the dominant source of their isotropic precipitation into the nightside ionosphere. *Planetary and Space Science*, *31*(10), 1147–1155. https://doi.org/10.1016/0032-0633(83)90103-4

Shi, R., Summers, D., Ni, B., Fennell, J. F., Blake, J. B., Spence, H. E., & Reeves, G. D. (2016). Survey of radiation belt energetic electron pitch angle distributions based on the Van Allen Probes MagEIS measurements. *Journal of Geophysical Research: Space Physics*, *121*, 1078–1090. https://doi.org/10.1002/2015JA021724

Shprits, Y. Y., Thorne, R. M., Friedel, R., Reeves, G. D., Fennell, J., Baker, D. N., & Kanekal, S. G. (2006). Outward radial diffusion driven by losses at magnetopause. *Journal of Geophysical Research*, *111*, A11214. https://doi.org/10.1029/2006JA011657

Sibeck, D. G., McEntire, R. W., Lui, A. T. Y., Lopez, R. E., & Krimigis, S. M. (1987). Magnetic field drift shell splitting: Cause of unusual dayside particle pitch angle distributions during storms and substorms. *Journal of Geophysical Research*, *92*(A12), 13,485–13,497. https://doi.org/10.1029/JA092iA12p13485

Su, Z., Zheng, H., Chen, L., & Wang, S. (2011). Numerical simulations of storm-time outer radiation belt dynamics by wave-particle interactions including cross diffusion. *Journal of Atmospheric and Solar-Terrestrial Physics*, *73*(1), 95–105. https://doi.org/10.1016/j.jastp.2009.08.002

Summers, D., Ni, B., & Meredith, N. P. (2007). Timescales for radiation belt electron acceleration and loss due to resonant wave-particle interactions: 2. Evaluation for VLF chorus, ELF hiss, and electromagnetic ion cyclotron waves. *Journal of Geophysical Research*, *112*, A04207. https://doi.org/10.1029/2006JA011993

Summers, D., Tang, R., & Thorne, R. M. (2009). Limit on stably trapped particle fluxes in planetary magnetospheres. *Journal of Geophysical Research*, *114*, A10210. https://doi.org/10.1029/2009JA014428

Tang, R., & Summers, D. (2019). Dependence of whistler mode chorus wave generation on the maximum linear growth rate. *Journal of Geophysical Research: Space Physics*, *124*, 4114–4124. https://doi.org/10.1029/2018JA026413

Tang, R., Summers, D., & Deng, X. (2014). Effects of cold electron number density variation on whistler-mode wave growth. *Annales Geophysicae*, *32*(7), 889–898. https://doi.org/10.5194/angeo-32-889-2014

Tsyganenko, N. A. (1995). Modeling the Earth's magnetospheric magnetic field confined within a realistic magnetopause. *Journal of Geophysical Research*, *100*(A4), 5599–5612. https://doi.org/10.1029/94JA03193

Wang, B., Su, Z., Zhang, Y., Shi, S., & Wang, G. (2016). Nonlinear Landau resonant scattering of near equatorially mirroring radiation belt electrons by oblique EMIC waves. *Geophysical Research Letters*, *43*, 3628–3636. https://doi.org/10.1002/2016GL068467

Wang, H., Ma, S., Hermann, L., Zhou, Y., & Dang, G. (2007). Field-aligned current distribution and response to interplanetary conditions during a superstorm—CHAMP observation. *Chinese Science Bulletin*, *52*(2), 248–258. https://doi.org/10.1007/s11434-007-0003-9

Wang, Z., Fu, H. S., Liu, C. M., Liu, Y. Y., Cozzani, G., Giles, B. L., et al. (2019). Electron distribution functions around a reconnection X-line resolved by the FOTE method. *Geophysical Research Letters*, *46*, 1195–1204. https://doi.org/10.1029/2018GL081708

West, H. I., Buck, R. M., & Walton, J. R. (1973). Electron pitch angle distributions throughout the magnetosphere as observed on Ogo 5. *Journal of Geophysical Research*, *78*(7), 1064–1081. https://doi.org/10.1029/JA078i007p01064

Xiao, F., Su, Z., Zheng, H., & Wang, S. (2010). Three-dimensional simulations of outer radiation belt electron dynamics including cross-diffusion terms. *Journal of Geophysical Research*, *115*, A05216. https://doi.org/10.1029/2009JA014541

Xiao, F., Yang, C., He, Z., Su, Z., Zhou, Q., He, Y., et al. (2014). Chorus acceleration of radiation belt relativistic electrons during March 2013 geomagnetic storm. *Journal of Geophysical Research: Space Physics*, *119*, 3325–3332. https://doi.org/10.1002/2014JA019822

Yang, C., Su, Z., Xiao, F., Zheng, H., Wang, Y., Wang, S., et al. (2016). Rapid flattening of butterfly pitch angle distributions of radiation belt electrons by whistler-mode chorus. *Geophysical Research Letters*, *43*, 8339–8347. https://doi.org/10.1002/2016GL070194

Yu, J., Li, L. Y., Cao, J. B., Reeves, G. D., Baker, D. N., & Spence, H. (2016). The influences of solar wind pressure and interplanetary magnetic field on global magnetic field and outer radiation belt electrons. *Geophysical Research Letters*, *43*, 7319–7327. https://doi.org/10.1002/2016GL069029

Yuan, C., & Zong, Q. (2013). Relativistic electron fluxes dropout in the outer radiation belt under different solar wind conditions. *Journal of Geophysical Research: Space Physics*, *118*, 7545–7556. https://doi.org/10.1002/2013JA019066

Yue, C., Bortnik, J., Thorne, R. M., Ma, Q., An, X., Chappell, C. R., et al. (2017). The characteristic pitch angle distributions of 1 eV to 600 keV protons near the equator based on Van Allen probes observations. *Journal of Geophysical Research: Space Physics*, *122*, 9464–9473. https://doi.org/10.1002/2017JA024421

Zhang, H., Khurana, K. K., Kivelson, M. G., Angelopoulos, V., Pu, Z. Y., Zong, Q. G., et al. (2008). Modeling a force-free flux transfer event probed by multiple Time History of Events and Macroscale Interactions during Substorms (THEMIS) spacecraft. *Journal of Geophysical Research*, *113*, A00C05. https://doi.org/10.1029/2008JA013451

Zhao, H., Friedel, R. H. W., Chen, Y., Reeves, G. D., Baker, D. N., Li, X., et al. (2018). An empirical model of radiation belt electron pitch angle distributions based on Van Allen probes measurements. *Journal of Geophysical Research: Space Physics*, *123*, 3493–3511. https://doi.org/10.1029/2018JA025277

Zhao, H., Li, X., Blake, J. B., Fennell, J. F., Claudepierre, S. G., Baker, D. N., et al. (2014). Peculiar pitch angle distribution of relativistic electrons in the inner radiation belt and slot region. *Geophysical Research Letters*, *41*, 2250–2257. https://doi.org/10.1002/2014GL059725

Zhao, H., Ni, B., Li, X., Baker, D. N., Johnston, W. R., Zhang, W., et al. (2019). Plasmaspheric hiss waves generate a reversed energy spectrum of radiation belt electrons. *Nature Physics*, *15*(4), 367–372. https://doi.org/10.1038/s41567-018-0391-6

Zhao, M. J., Fu, H. S., Liu, C. M., Chen, Z. Z., Xu, Y., Giles, B. L., & Burch, J. L. (2019). Energy range of electron rolling pin distribution behind dipolarization front. *Geophysical Research Letters*, *46*, 2390–2398. https://doi.org/10.1029/2019GL082100

Zhong, Z. H., Zhou, M., Tang, R. X., Deng, X. H., Turner, D. L., Cohen, I. J., et al. (2020). Direct evidence for electron acceleration within ion-scale flux rope. *Geophysical Research Letters*, *47*(1). https://doi.org/10.1029/2019GL085141

Zhou, M., Deng, X., Ashour-Abdalla, M., Walker, R., Pang, Y., Tang, C., et al. (2013). Cluster observations of kinetic structures and electron acceleration within a dynamic plasma bubble. *Journal of Geophysical Research: Space Physics*, *118*, 674–684. https://doi.org/10.1029/2012JA018323

Zhou, M., Deng, X. H., Zhong, Z. H., Pang, Y., Tang, R. X., el-Alaoui, M., et al. (2019). Observations of an electron diffusion region in symmetric reconnection with weak guide field. *The Astrophysical Journal*, *870*(1), 34. https://doi.org/10.3847/1538-4357/aaf16f